



## **Master's thesis**

Patsrikasem Vanitcharenthum

# **Probing the Standard Cosmological Model with Gravitational Waves**

August 2023

Supervisor: Asst. Prof. Jose Maria Ezquiaga Bravo

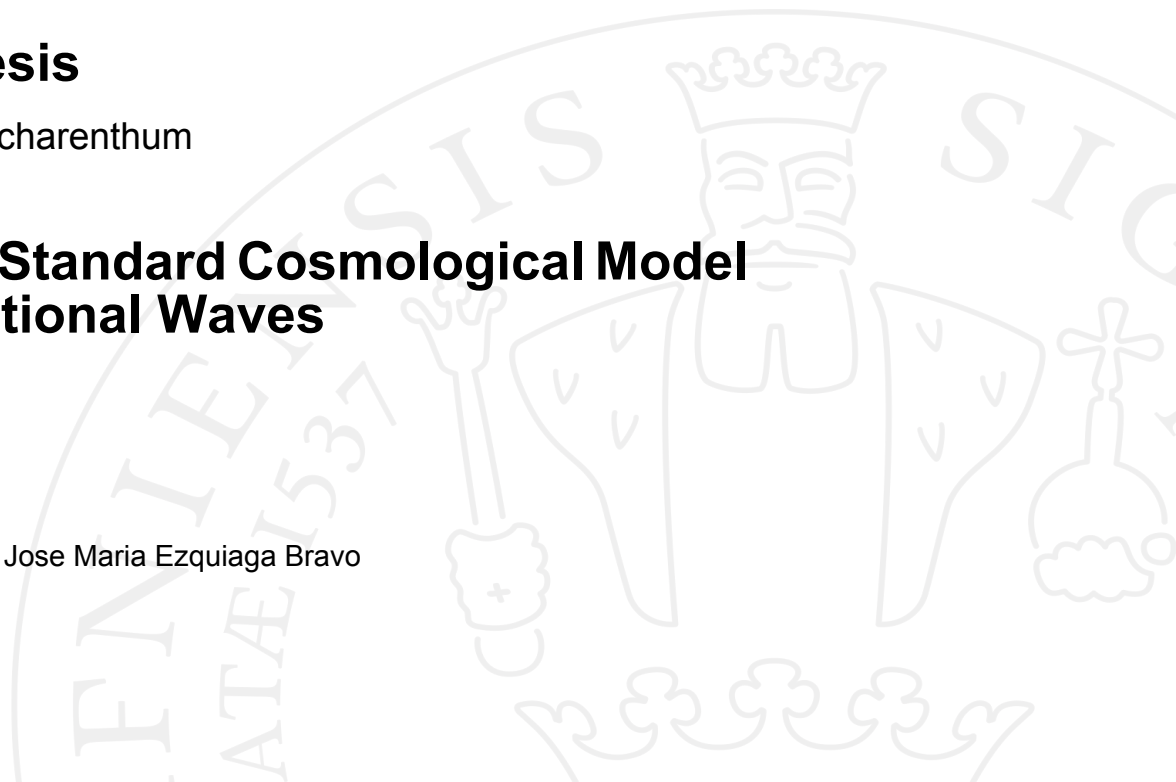


# Table of content

<b>1</b>	<b>PART I: Gravitational wave detection</b>	<b>3</b>
1.1	Introduction . . . . .	3
1.1.1	What are gravitational waves ? . . . . .	3
1.1.2	What sources can we expect? . . . . .	4
1.1.3	How can we detect them . . . . .	5
1.2	Theory . . . . .	6
1.2.1	Gravitational wave signal . . . . .	6
1.3	Methodology . . . . .	8
1.3.1	Signal to Noise Ratio . . . . .	8
1.3.2	Source Population . . . . .	10
1.3.3	Selection Bias . . . . .	12
1.3.4	Detectability . . . . .	13
1.3.5	Detection Rate . . . . .	14
<b>2</b>	<b>PART II: Bayesian Inference and Cosmology</b>	<b>18</b>
2.1	Bayesian Inference . . . . .	18
2.2	Methodology . . . . .	19
2.2.1	Cosmology in the algorithm . . . . .	19
2.2.2	Constraining $\Omega_{m0}$ and $H_0$ . . . . .	20
2.2.3	Constraining $\Omega_{m0}$ and $w_{DE}$ . . . . .	20
2.2.4	Constraining $\Omega_{m0}$ and $w_{DM}$ . . . . .	23
2.2.5	Constraining $\Omega_{m0}$ and $\Omega_{k0}$ . . . . .	24
2.3	Results and Analysis . . . . .	24
2.4	Possible Improvement . . . . .	25
<b>3</b>	<b>Conclusion</b>	<b>25</b>
<b>4</b>	<b>Appendix</b>	<b>27</b>

## Abstract

Gravitation waves from coalescence of binary black holes are one of the most fascinating events of astrophysics. They are one of the newest proven physics that are now widely studied, due to the rich cosmological information that could be extracted from these signal. Hence why we have chosen to utilise them to inspect the standard model of cosmology, as well as the population distribution of the sources themselves.

In part I of this master thesis, the focus would be on the detection of gravitational waves, and what affects the detection rate. This includes studying the Signal to Noise Ratio, and analysing the sensitivities of ground based detector of different generations. We simulated merging events by inverse transform sampling from theoretical population distribution. Ultimately we estimated the number of expected detection per year for different detectors such as LIGO O3,O4, and VIRGO O5. Whereas in part II, we explored how these gravitational wave signals could be used to infer cosmological parameters. By using bayesian inference and MCMC algorithm we could constrain  $\Omega_{m0}, w_{DE}, w_{DM}$  and  $h_0$ , as well as parameters of mass and redshift distribution for binary black hole population.

# 1 PART I: Gravitational wave detection

## 1.1 Introduction

### 1.1.1 What are gravitational waves ?

When massive objects in the universe such as black holes or neutron stars orbits around each other, they create ripple in space time that travel at the speed of light; these ripples are called gravitational waves. These waves can travel through the universe without being obstructed, allowing observers to deduce the properties of the source as well as studying those that are far into the early star formation era[1]. The limit is our detectors. This, again, is why gravitational waves are studied widely in many astrophysics field.

Gravitational waves were first predicted by theory of general relativity, which stated that they are the wave solution of the linearised vacuum Einstein's equation;

$$\square h_{\mu\nu} = 0 \tag{1}$$

Where the solution is of form:

$$h_{\mu\nu} = A_{\mu\nu} \exp^{ik_\rho x^\rho} \tag{2}$$

Where  $A_{\mu\nu}$  and  $k_\rho$  are constants. Imposing conditions (i.e.  $A_{\mu\nu} = A_{\nu\mu}, A_{\mu 0} = 0$ ) to these constants, the solution then corresponds to a small perturbation of the  $h_{\mu\nu}$  in Minkowski metric as;

$$h_{\mu\nu} = Re[A_{\mu\nu}exp^{ik_\rho x}] \quad (3)$$

The consequences of these waves travelling through space that should be considered is how they affect motionless test particles. In practice- the effect of gravitational wave are best demonstrates on multiple test masses, and how they move relative to each other in 2D plane. Hence we get that  $h$  has 2 possible mode according to the condition of  $A_{\mu\nu}$  earlier, and imposing this into the defined wave solution:

$$h_{11} = -h_{22} = B_1cos(\omega t + \chi_1) \quad (4)$$

$$h_{12} = h_{21} = B_2cos(\omega t + \chi_2) \quad (5)$$

We can formulate proper distance between test particles, when they lie perpendicular to the direction of wave propagation as [2]:

$$L(t) = L_0 \left[ 1 + \frac{1}{2}h_{11}(t)cos(2\theta) + \frac{1}{2}h_{12}(t)sin(2\theta) \right] \quad (6)$$

By investigating particles on each axis  $x_1x_2$  (i.e. the spatial x and y axis) on each mode;  $h_{11}$  and  $h_{12}$  independently, one could see that the movement effect is rotated 45 degree from each other. To explain this more clearly- particles along  $x_1$  move towards each other, while those along  $x_2$  move away from each other in the case of  $h_{11}$ . In the case of  $h_{12}$ , particles behave the same way but the particles along  $x_1$  move in  $x_2$  direction and vice versa; resulting in an affect that is 45 degree rotated from  $h_{11}$  mode. Hence why we refer to these two modes as the polarisation of gravitational waves, and in this project we will refer to them as  $h_+$  and  $h_\times$ .

### 1.1.2 What sources can we expect?

Gravitational wave range is a broad spectrum that could be generated from range of sources; from the big bang to the orbit of massive objects around each other. In general, (any) oscillating mass with asymmetry could radiate gravitational wave. It is analogous to how electromagnetic wave propagate, but the gravitational counterpart requires 'quadrupole' expansion of mass. [3]

The properties of the source such as its mass and size of the system dictates what frequency the gravitational wave emitted would be. For the most extreme source such as the

big bang, gravitational wave generated would have a frequency on the scale of  $10^{-16}$  Hz. On the other end of the spectrum, we have smaller sources such as binary neutron star or supernovae which would generate about  $10^3$  Hz. Another important factor to consider is how far away the source is- because if they are in cosmological distances, the expansion of the universe would stretch the wave, resulting in lower frequency upon arrival to a detector.

So what kind of sources are more likely to be detected by the detector of our interest? Looking at LIGO's sensitivity in the current generation(O3, O4): they can detect between 10-5000 hz, this means that we could also detect coalescing blackholes with higher masses if they are from cosmological distances, then they could land within LIGO's detection window.

### **1.1.3 How can we detect them**

As explained previously, gravitational wave stretch and squeeze matter when they pass through. This means that using a physical ruler to measure the distance perturbation simply would not work as the very measurement equipment would be stretched and squeezed at the same time.

Fortunately, physicists have discovered multiple ways to circumvent this. There are 3 main types of detectors[4]. For ground based detectors, they can either use resonant mass detectors or interferometers, and space based. The first kind of gravitational wave detector was in fact, a resonant mass one. They are made up of two aluminium bars, which oscillate as gravitational wave passes through and transfer energy to them. This could be measured by using a transducer that convert stress into electricity and amplifies it.

Meanwhile, detectors such as LIGO or VIRGO utilize light laser interferometer, which gives better sensitivity than resonant mass detectors, as they are rid of thermal oscillation within the metal. An interferometer consists of a pair of interfering light that reflect them back and forth along each perpendicularly crossing 'arms'. The length of each arms are equal such that the light are in phase with each other. In an event where a gravitational wave passes through, it will vary the distance of each arm, causing time delay of the light signal, resulting in signals that are in and out of phase. These signal are converted into the amplitude of gravitational wave. Detectors like LIGO can measure changes in distances of order  $10^{-18}$  meter [5], but the new generations of detector such as Cosmic Explorer[1] would have even higher sensitivity - with 10 times that of LIGO.

Moreover, it is also possible for detectors to be space-based. The example is the future telescope, LISA( Laser Interferometer Space Antenna). The advantages of operating in space are the fact that the distance scale for the detectors is much greater, and that there's much less source of noise vibration. These allow for higher sensitivity and detection of lower frequency band of gravitational wave than LIGO/Virgo. However in this project we will only

focus on properties and capabilities of ground-based detectors.

## 1.2 Theory

### 1.2.1 Gravitational wave signal

When a black hole or neutron star pair orbit around each other in a quasi-circular motion, they lose their energy in a form of gravitational wave. The inspiral phase is refer to when the binary release gravitational radiation, and shrink in orbital radius. This continues until they reach their Innermost Stable Circular Orbit(ISCO). Then they enter the plunging phase, and finally ending with the objects combining into one. During these processes, the physics of their motion can change drastically, so the formulation of gravitational waveform at a relevant phase is important. In this project, we are interested in gravitational waves released by inspiralling blackhole binaries. Such waveform is valid up until the ISCO, and is expressed with  $h_+(t)$  and  $h_\times(t)$  as the following:

$$h_+(t) = \frac{1}{r} \left( \frac{GM_c}{c^2} \right)^{5/4} \left( \frac{5}{c\tau} \right)^{1/4} \left( \frac{1 + \cos^2(i)}{2} \right) \cos[\phi(\tau)] \quad (7)$$

$$h_\times(t) = \frac{1}{r} \left( \frac{GM_c}{c^2} \right)^{5/4} \left( \frac{5}{c\tau} \right)^{1/4} \cos(i) \sin[\phi(\tau)] \quad (8)$$

Where  $\tau$  is the time to coalescence measured by observer

$$\tau = t_{coal} - t_{obs},$$

$i$  = viewing angle from ground to source

$r$  = physical distance from source

$\phi$  = angular phase

$M_c = \mu^{3/5} m^{2/5} =$  chirp mass,

$\mu = \frac{m_1 m_2}{m_1 + m_2} =$  reduced mass and  $m = m_1 + m_2$ ,

There also exists the Fourier transformed version of equations (7) and (8) such that they're a function of the frequency:

$$\tilde{h}_+(f) = A e^{i\Psi_+(f)} \frac{c}{r} \left( \frac{GM_c}{c^3} \right)^{5/6} \frac{1}{f^{7/6}} \left( \frac{1 + \cos^2(i)}{2} \right) \quad (9)$$

$$\tilde{h}_\times(f) = A e^{i\Psi_\times(f)} \frac{c}{r} \left( \frac{GM_c}{c^3} \right)^{5/6} \frac{1}{f^{7/6}} \cos(i) \quad (10)$$

Where  $A = \frac{1}{\pi^{2/3}} \left( \frac{5}{24} \right)^{1/2}$  and is a constant.

By looking at how frequency is evolved, it can be seen that as coalescence is approached,

frequency and amplitude of the wave increases until two bodies collide - this phenomenon is referred to as 'chirping'. As also mentioned earlier, the inspiral phase ends when the ISCO is reached. So the maximum possible frequency produced by a binary is :

$$f_{max} = \frac{1}{3\sqrt{6}(2\pi)} \frac{c^3}{Gm} \quad (11)$$

and we can see that this is inversely proportional to the combined mass of the system,  $m$ . This will be important later on in the method section, as we could use such relationship to compare waveform with different masses.

So far we have the standard gravitational waveform equations - now we can take into account the effect of the expanding universe on the detected gravitational wave. This is necessary because modern GW detectors can detect signal from sources that are a multiple Gpc away, where the waveform will be redshifted significantly.

That means we must also use an appropriate metric to modify our gravitational waveform equations of such scale. In this case it is the FRW (Friedmann-Robertson-Walker) metric, which states that the universe is approximately homogenous and isotropic on a Gpc scale. The coordinates in FRW metric consists of the time,  $t$ , and the spatial coordinates  $r$ ,  $\theta$  and  $\phi$ . As well as the scale factor,  $a(t)$ . By considering how radiation spread from a source, in an expanding universe, we could formulate the luminosity distance in relation to the scale factor as:

$$d_L = (1 + z)a(t)r \quad (12)$$

Integrating definition of  $r$  in time, one gets  $d_L$  expressed as integral of the hubble parameter:

$$d_L(z) = c(1 + z) \int_0^z \frac{dz'}{H(z')} \quad (13)$$

which describes the whole history of the expansion of the universe. The quantity  $d_L$  could also be obtained from observables; by using observed flux  $F$ , and intrinsic luminosity,  $L$ , which could be determined from a standard candle.

As for the gravitational waveform, it was formulated by considering the propagation of the scalar perturbation  $\phi$ . Where the propagation equation is of  $\square\phi = 0$ . By solving this in FRW metric, one obtain equations describing perturbation similar to equations (7) and (8) but with  $1/ra(t)$ , or  $1/d_L(z)$  instead of  $1/r$ .

$$h_+ = h_c(\tau) \frac{1 + \cos^2 i}{2} \cos[\phi(\tau)] \quad (14)$$

$$h_\times = h_c(\tau) \cos i \sin[\phi(\tau)] \quad (15)$$

Where  $h_c(\tau) = \frac{4}{d_L(z)} \left( \frac{GM_c(z)}{c^2} \right)^{5/3} \left( \frac{\pi f(\tau)}{c} \right)^{2/3}$ , and  $f$  is the frequency of GW.

Finally, there are a few more important changes to consider when taking gravitational wave signal from cosmological distances. For example, mass inferred in observer's frame is different to that in the source frame:

$$M_c^{observer} = M_c^{source} \times (1 + z) \quad (16)$$

As well as frequencies, over cosmological distance would be stretched out from the expansion:

$$f^{observer} = \frac{f^{source}}{1 + z} \quad (17)$$

These were taken into account when we made the simulation.

### 1.3 Methodology

Content beyond this point is about the work done in part I of the project, which concerns the detection of gravitational wave and what affect the rate of detection. To study this, a simulation of gravitational wave signals from binaries was needed. In which a python program utilising LALsimulation was written. How the waveform generator program works is that, it takes input such as masses of the binary, redshift, angular positions, spin, etc. to generate wave forms in polarisation  $h_+$  and  $h_\times$ . The simulation also used IMRphenomXAS[6] as a waveform model. As mentioned before, the waveform equations in the previous section are not valid beyond ISCO. Hence why a model IMRPhenomXAS was used, because it provides a (non-precessing) gravitational waveform up to the coalescence.

Then in the later part of the methodology section, it will be shown that the parameters of the sources; mass ( $m$ ) and redshift ( $z$ ), were selected from theoretical distributions to simulate coalescing events, and then used to determine detectability of the detector, and the detection rate per year.

#### 1.3.1 Signal to Noise Ratio

The first important quantity used for determining whether a gravitational wave signal is detected by LIGO is the SNR (we require that SNR should be higher than 8 to have a detected signal). This is defined as  $\frac{S}{N}$  from the following expression[7]:

$$\left( \frac{S}{N} \right)^2 = 4 \int_0^\infty df \frac{|h(f)|^2}{S_n(f)} \quad (18)$$

Where  $S_n(f)$  is the Power Spectral Density (PSD) or also known as noise spectral density, has the unit of  $\text{strain}^2/\text{Hz}$ . It is defined as the squared of amplitude of the strain, as measured by the equipment for each frequency from highest to lowest that it can detect. We could acquire these amplitude from LIGO's publicly available data.

For  $|h(f)|^2$ , this is equal to the square of GW signal amplitude. In a general case, this could be the actual detected signal. In this project, since we are simulating events, we obtained  $h(f)$  from the gravitational wave form generator program mentioned above. Since the program generates strain in  $h_+$  and  $h_\times$ , we included the antenna pattern function  $F_+$  and  $F_\times$  for each polarisation such that:

$$h = F_+h_+ + h_\times F_\times \quad (19)$$

Where each antenna pattern function is defined as:

$$F_+ = \frac{1}{2}(1 + \cos^2 \theta) \cos 2\phi \cos 2\psi - \cos(\theta) \sin 2\phi \sin 2\psi \quad (20)$$

$$F_\times = \frac{1}{2}(1 + \cos^2 \theta) \cos 2\phi \sin 2\psi + \cos(\theta) \sin 2\phi \cos 2\psi \quad (21)$$

Antenna pattern values ranges from minimum at 0, to a maximum at 1. They describe a detector's response as a function of angular directions;  $\theta$  = angle from zenith,  $\phi$  = azimuthal angle from detector's x arm to that of the source, and  $\psi$  = angular rotation in the sky's plane(polarization). Note that when we use these function in the simulation, all angular direction are set to 0 to obtain a maximum possible response of the detector; this is when the source is directly overhead of the detector. Finally, using  $h$  from equation (19), we can obtain  $h(f)$  needed to calculate the SNR equation (18), from  $h$  and its complex conjugate as:  $h(f) = h^*h$ .

Another great application of SNR that we have used was to determine which frequency range is relevant for our detector. Given a specific mass and redshift distribution of the source, we looked at two extreme cases: the high  $f_{max}$ , and the low  $f_{max}$ . Essentially, a combination of a lowest redshift and a lowest mass in the range, would give the highest  $f_{max}$ . Then of course the lowest  $f_{max}$  would be created from a binary with the highest redshift and the lowest mass in the range. What this does to the SNR is that, the higher  $f_{max}$  would reach peak SNR at higher frequency, while the lower extreme would reach peak SNR at lower frequency. This is demonstrated in figure[1], which is a graph of cumulative SNR at each frequency. It can be seen on this graph that 'peak SNR' for each cases is reached where the lines stopped rising.

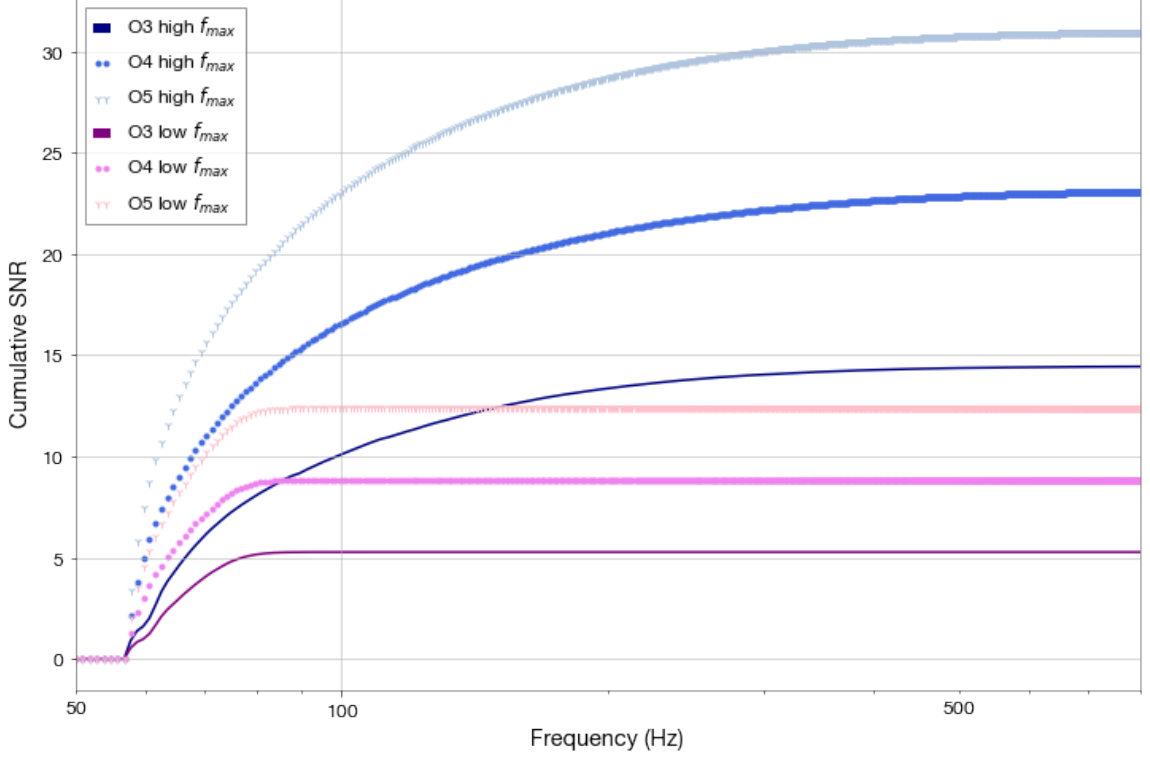


Figure 1: Cumulative SNR for different detector generations, where its signal came from a high extreme of  $m = 2M_{\odot}$  and  $z = 0.1$  (blue lines), and low extreme of  $m = 5M_{\odot}$ , and  $z = 5$  (purple lines)

### 1.3.2 Source Population

As mentioned in the beginning of method section, that we had to select a sample of sources with masses( $m$ ) and redshift( $z$ ) from a known probability distribution. The way to select them is not entirely random, but to do an inverse transform sampling.

Firstly, we need probability distributions of binary blackholes. In redshift, this is a peaked distribution given as :

$$p(z) \propto \frac{(1+z)^{\alpha}}{1 + \left(\frac{1+z}{1+z_p}\right)^{\alpha+\beta}} \quad (22)$$

and it is based off of a curve fitting the plot of a star formation rate from [8]. Which makes sense, as the occurrences of stellar mass blackholes should somewhat follow the star formation. In equation(22),  $\alpha$  and  $\beta$  are constants controlling the gradient of the left side and the right side of the slope, respectively. Finally,  $z_p$  is the value of redshift where the

probability is the highest within that distribution.

Secondly, for the probability distribution in the mass, we used a powerlaw + peak distribution that is similar to Abbot et al [9]. As the name suggests, the distribution is made by combining a powerlaw and a 'peaked' distribution, which is a gaussian curve. A factor  $f_{peak}$  would control how much fraction of either powerlaw or gaussian would be more prominent in the over all distribution:

$$p(m) \propto \left[ f_{peak} \times (gaussian) + (1 - f_{peak})(powerlaw) \right] \times FILTER \quad (23)$$

Where the mass FILTER is a function that is applied to  $p(m)$  when  $m < M_{min}$ , and  $m > M_{max}$  to keep the function in its shape depending on value of  $M_{min}$  and  $m > M_{max}$ . More about the filter function will be elaborated in the Appendix.

The powerlaw function is:

$$\left( \frac{1 + \alpha}{(M_{PL,min})^{\alpha+1} - (M_{PL,max})^{\alpha+1}} \right) m^\alpha \quad (24)$$

Where  $M_{PL,min} = 2$  and  $M_{PL,max} = 150$  are just min and max mass value specific for this function. With  $\alpha$  as spectral index. Note that this  $\alpha$  is obviously different from that of equation(22).

Since the sources are coalescing binary we could have also taken into account the ratio  $q$  between masses  $m_1$  and  $m_2$ , but for simplicity of the simulations, we have decided to make  $m_1 = m_2$ . So from this point on, any mention of  $m$  refers to mass of one of the blackhole in a binary, and not combined mass.

To make sure our distribution in mass and redshift is as close to the literature[9] as possible, we compared the plot for their distribution in  $m$  and  $z$  with those from ours, and adjust our parameter to match their distributions. These are shown in fig[2] and fig[3] respectively.

The parameters we obtained by comparing the plots are as following:

$\alpha_z = 2.7, \beta = 2.9, z_p = 1.9$  for  $p(z)$ , and

$\alpha = -2.01, \sigma = 2.65, \mu = 33.73, M_{min} = 8, M_{max} = 86.85, f_{peak} = 0.02$  for  $p(m)$ .

After we obtained the appropriate probability distribution for  $m$  and  $z$ , we could use them in the inverse transform sampling process. This was done by turning the probability distributions into a cumulative probability distribution. Then randomly picked out numbers between 0 to 1 from the cumulative distribution. Even though the randomly picked numbers may have been generated from a uniform random, but when they were plugged into our cumulative distribution functions, they will behave according to the original distribution.

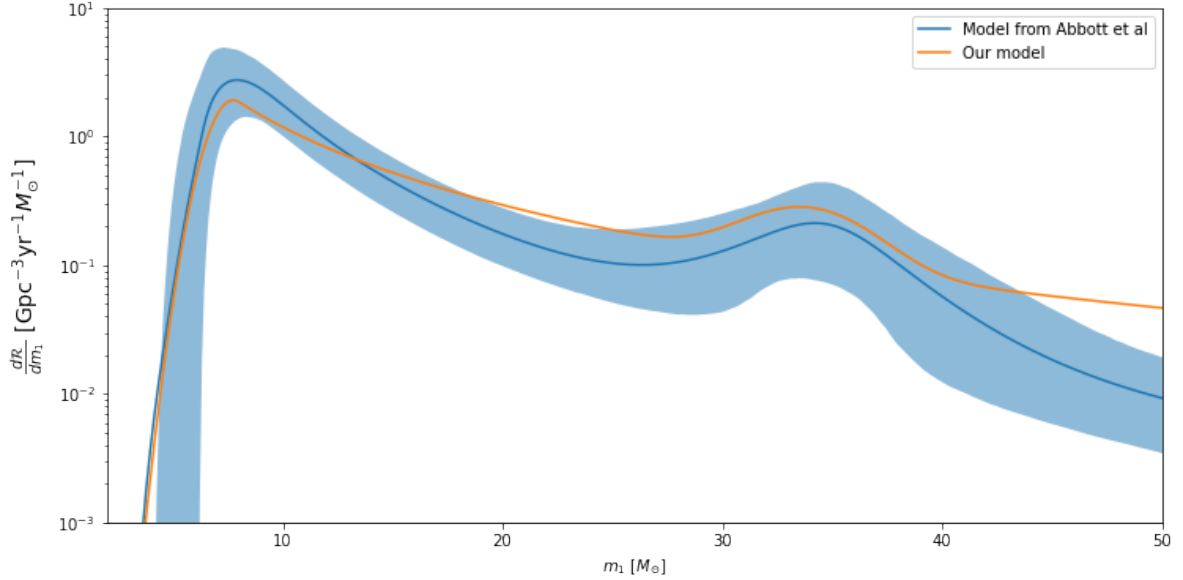


Figure 2: Plot shows differential merger rate as a function of primary mass ( $m_1$ ) where the distribution is governed by powerlaw peak model, with the light blue area as the 90% credible interval. Blue solid line is from literature, and is compared with our mass distribution (orange line) that is given in expression(23)

Hence, this was how we simulate random events that followed the probability distributions. This is demonstrated in fig[4]: The solid purple line in the left plot and the solid dark blue line in the right plot shows the theoretical model we used for distribution of sources in mass and redshift respectively. We can see that the randomly generated data (red and blue histogram) follows the solid line strictly in both plots.

### 1.3.3 Selection Bias

Next, these random events have to be determined whether they would be detected by LIGO. As mentioned in the previous section that the requirement for a signal to be detected is to have  $\text{SNR} > 8$ , After we acquired the detected data, we plotted them against the generated data in histogram plots. This is useful as it demonstrates clearly the distribution of the generated signal and how the distribution of detected signal differs from that.

This effect is due to the fact that detectors are able to see sources with some specific properties better. Here, we can see that these are those with higher masses, and lower redshift. This happens regardless of what the actual distribution of source is out there.

As demonstrated in the histogram plots (fig[4]). For the distribution in mass, the detected

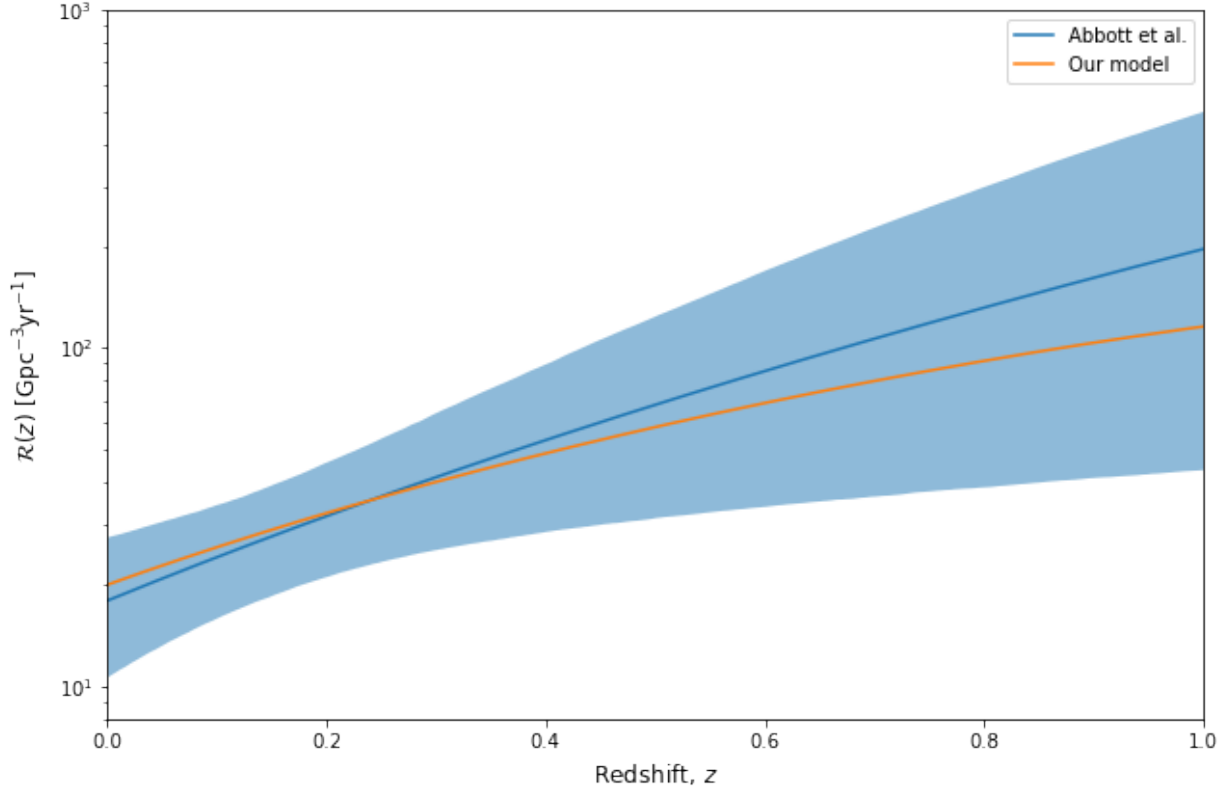


Figure 3: (Blue solid line) Merger rate as a function of redshift,  $R(z)$ , with the light blue area as the 90% credible interval. (Orange line) Plot of 'our model', that is according to the probability distribution given in equation(22).

data shows a peak in the higher mass region, even though the original distribution peaks in the lower region. Also in the redshift distribution counterpart, the detected signal peaks in the lower redshift region instead of following the generated distribution.

### 1.3.4 Detectability

Other than using SNR to determine whether a source could be detected, we also have taken into account the cumulative distribution function of the antenna pattern,  $P(\omega)$ . This is defined as the probability of a signal from a source having SNR of at least  $\rho$ . The parameter governing the function is  $\omega$ , and it is a ratio of:

$$\omega = \frac{\rho_{thresh}}{\rho_{opt}} \quad (25)$$

Where  $\rho$  is the value of SNR of a source. Here, the threshold SNR, or  $\rho_{thresh}$  is set as 8[11]. The optimal SNR,  $\rho_{opt}$ , is the measured SNR from each of our generated signal. This works

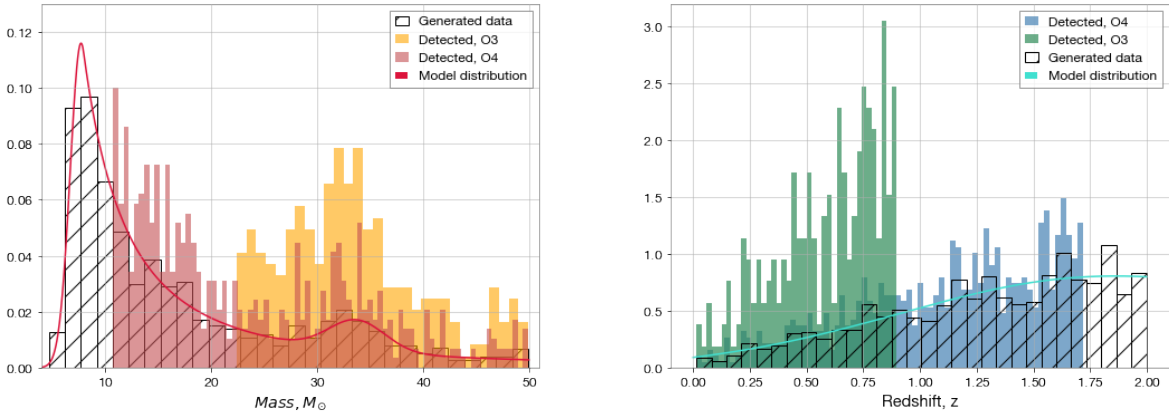


Figure 4: Histogram of generated data VS detected data. (Left) Shown data selected from probability distribution in mass, with  $z$  kept constant at 0.5, to demonstrate the effect clearer. (Right) Data selected from distribution in  $z$  while  $m_1 = m_2$  kept constant at 50. Both also showed how much of them would be detected if the detector was LIGO O3 and O4. All histograms are plotted with normalised density.

because we have set the orientation of each sources to optimum- i.e. all angular position = 0, as mentioned in previous section. After computing  $\omega$ , we then obtained values of the corresponding  $P(\omega)$  by interpolating from table of antenna pattern provided in a study by Chen et al.[10]. Where this table is universal for any single detector. The significance of using this  $P(\omega)$  is so that there is a 'smoothed' transition of probability between a signal being detected: 1, and not detected: 0. A plot of  $P(\omega)$  function is in the Appendix.

After generating number of sources by using inverse transform sampling and calculate their SNR, each of their corresponding value of  $P(\omega)$  was also determined. Finally, we have plotted 2D detectability map by using  $P(\omega)$  values in the function of both mass and redshift fig[5], for different generations of detectors. It can be seen that as we goes from LIGO O3,O4, and to VIRGO O5, the detectibility increases into higher mass and higher redshift region, as expected (Plots in [5] with sensitivity of O3 and O4 agreed with that presented in fig.5 of [11]). There we also extend the mass range into 500, to show where the detectibility peaks and disappear, as mass becomes very large.

### 1.3.5 Detection Rate

We were interested in determining the rate of detection,  $\frac{dN}{dt}$  of gravitational wave signals from coalescing blackhole binary by our detectors, per year. To formulate this; we had to take into account the cosmology- that is, the expansion of the universe would affect the signal that could reach us. Combining with all the different factors that affect the detection

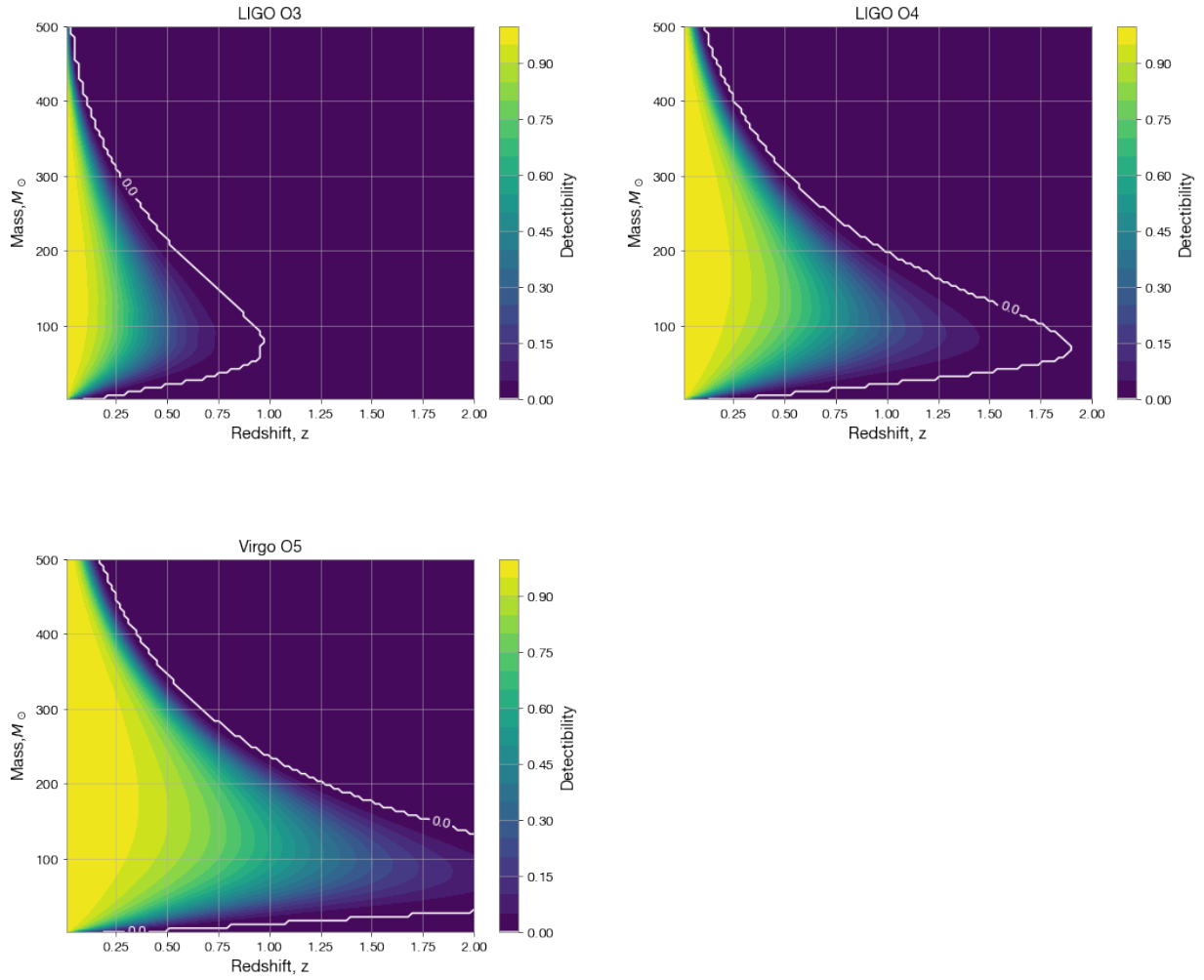


Figure 5: Three contour maps showing detectability for different mass and redshifts, with sensitivity of LIGO O3, O4, and VIRGO O5. The white line shows where detectability goes to 0 in each plots.

that we have computed so far, we could estimate the detection rate. Therefore, this is[11] :

$$\frac{dN}{dt} = \int \int dz dm \frac{R(z)}{1+z} \frac{dV_c}{dz} P_{det}(z, m) p(m) \quad (26)$$

It consists of the merger rate density per comoving volume,  $R(z)$ , co-moving volume,  $\frac{dV_c}{dz}$ , probability of detection,  $P_{det}$ ; which we have worked out previously, and the probability distribution of sources in terms of mass,  $p(m)$ .

The probability distribution of sources in terms of redshift is already included in the definition of the merger rate. This is because it is defined as the number of merging (which

depends on  $z$ ) per volume of space per time(year). To write this out:

$$R(z) = R_0 N c_0 p(z) \quad (27)$$

Where  $R_0$  is the merger rate per year at redshift  $z = 0$ . This constant was determined by comparing our model with that from Abbot et al[9], which we found it to be  $R_0 = 18Gpc^{-3}yr^{-1}$ . Then  $N$  is the normalising constant for  $p(z)$ , and  $c_0$  is a factor that ensures we recover  $R(0)$  when  $z = 0$  in equation(27).

To make sure the simulation we made so far was is rid of human error - we needed to check for convergence. By increasing number of data points, we expect the result to converge to a specific value of detection rate. This also means that the algorithm reaches better and better approximation to a solution. We did this by increasing the dimension of  $m$  and  $z$  matrix that we input in the integral (equation26) -until the output converges. We found that, by using LIGO O3 sensitivity, we obtained the rate of  $\approx 362$  detections per year. Note that when we calculated the rate by integrating directly with equation (26), the input mass and redshift matrix were to be uniformly generated, for the integral to be valid.

We have also calculated the rate of detection per year with different detector sensitivities with the method above. The rates were taken when the program has converged enough such that the consecutive results are accurate to the last digit.

LIGO O3	LIGO O4	VIRGO O5	Einstein Telescope	Cosmic Explorer
362	965	1745	8030	9119

Table 1: Estimated rate of detection per year for different detectors

There is also another way to calculate rate from data that are randomly selected (i.e. by using our distributions and inverse transform sampling). This was done by calculating an expectation value. This works because we treated the integral in (26), which is evaluated in  $dz$  and  $dm$ , as :

$$\left\langle \frac{R_0 N c_0 p(z)}{1+z} \frac{dV_c}{dz} P_{det} \right\rangle_{z,m \in p(z)p(m)} \quad (28)$$

by using Monte Carlo integration:

$$\int f(x)p(x)dx \approx \langle f(x) \rangle_{x \in p(x)} \quad (29)$$

Equation (28) is then an expectation value of the integrand of (26), where  $m$  and  $z$  are generated from their probability distribution.

With this method, we also reached the converged value of detection rate per year as  $\approx 340$ . A disadvantage of using the expectation value method is that it converges slightly slower than the integration method. The solution from both methods may seem very high, but they are very close to each other.

There are multiple reasons why the rate calculated is much higher than the past observes (76 merging compact binaries with GWTC-3 [9]). These factors are due to the way we wrote the simulation.

First of all, we have set the sources' angular position and orientation to be in the detector's maximum sensitivity. This, combined with the fact that we have set the mass within a binary such that  $m_1 = m_2$ , which gives higher amplitude than any other ratio. Secondly, we did not take into account the selection bias- as this could be tricky to try to model, and counter it. Because unlike the uncertainty that would decrease would number of measurements, a bias would remain constant regardless.[12] . Lastly, the mechanism we used to decide which signal would be detected was by using SNR. However in real-life detectors, they also use a false alarm rate to eliminate uncertain measurements that could be caused by noise.

## 2 PART II: Bayesian Inference and Cosmology

In this section, we used bayesian inference to constrain multiple cosmological parameters such as  $H_0, \Omega_{m0}, w_{DM}, w_{DE}, \Omega_{k0}$ , together with the mass and redshift distribution parameters:  $M_{min}, M_{max}, \alpha, \mu, \sigma$  and  $\alpha_z$  (refer to Source Population section). These parameters were used to generate the mock data, that were treated as detections. The point of this method is to generate detections by a modern ground based detectors, and so we could see how much can we constrain, and how much error can we expect.

The building of the simulation in this part utilised the concepts we studied in the first part. For example, the mock data was generated by doing the inverse transform sampling method on the probability distribution function in  $m$  and  $z$  of coalescing blackholes. As well as the knowledge of how properties of the source would change due to the expansion, such as source's mass, which had to be changed to that in observer's frame.

### 2.1 Bayesian Inference

It is undeniable that, the bayesian approach to statistic is invaluable in all sciences in modern times. As apposed to a frequentist approach, where one obtain inference by maximising the frequency of measurements- This has its shortcoming. What made bayesian statistic[13] different is that it describes hypothesis and data as a probability distribution, and accounts for their uncertainty. This brings us to the Bayes' Theorem- which is the heart of the bayesian inference algorithm. The formula states the relationship between the posterior and the combination of prior knowledge and observations. This can be expressed as:

$$p(\theta|x) = \frac{p(x|\theta)p(\theta)}{p(x)} \quad (30)$$

Where  $p(\theta|x)$  = posterior

$p(x|\theta)$  = likelihood function

$p(\theta)$  = prior (knowledge about  $\theta$ )

$p(x)$  = evidence or observation

Generally for a model,  $x$  are data generated from a probability distribution with an unknown parameter  $\theta$ . After data  $x$  is generated, a prior can then be updated. This step is repeated and a posterior distribution is better determined.

In our program, we coupled this with a Monte Carlo Markov Chain (MCMC) algorithm. It uses multiple walkers that can simultaneously explore a probability space within a given range. With each iteration steps, they check if the likelihood of the new value is better, then update the prior and takes the path with better likelihood. As a result, they move closer

and closer towards a value with best outcome.

## 2.2 Methodology

In order to operate the bayes theorem in a simulation, we needed to generate 'observations' or detections from our source's probability distribution. Then compare those with the data from 'fiducial' universe of known cosmology. Below is the table of cosmological fiducial values used for the bayesian inference program. For  $H_0$  and  $\Omega_{m0}$ , we obtained from *astropy.cosmology*

$H_0$	$\Omega_{m0}$	$w_{DE}$	$w_{DM}$
67.66	0.30966	-1	0

Table 2: Cosmological fiducial values used as priors for the bayesian inference .

based from Plank 2018[14] measurements. The  $\Omega_{m0}$  here is slightly different from the paper as *astropy* excludes heavy neutrinos from  $\Omega_{m0}$ .

### 2.2.1 Cosmology in the algorithm

In the initial stage, the free parameters for the bayesian inference code only consisted of those governing the distribution of the source, and those for cosmology were only  $H_0$  and  $\Omega_{m0}$ . There was no curvature term in the simulation, and the cosmology model is that of  $\Lambda_{CDM}$ . Therefore, in order to introduce  $w_{DE}$ ,  $w_{DM}$  or  $\Omega_{k0}$ , changes needed to be made to any expressions concerning such cosmology in the simulation.

Secondly, the energy term. This is governed by the density parameter of cosmological fluids; dark energy, (baryonic and dark)matter, and radiation, and density parameter due to curvature.

$$E(z) = \frac{H(z)}{H_0} = \sqrt{\Omega_{DE} + \Omega_m + \Omega_R + \Omega_k} \quad (31)$$

Note that here, we have taken  $\Omega_{R,0} \approx 0$ , since we know from CMB that the radiation density is very low in current time( $\sim 10^{-5}h^2$ ). The present universe is dominated by dark energy, and second to that is matter- so radiation is negligible in comparison.

We also introduced another new parameter,  $w$  that is the constant in the equation of state of the cosmological fluids:

$$p = w\rho \quad (32)$$

Where each fluid type have different  $w$  such that their equation of state are, for example:  $p = -\rho$  for dark energy, and  $p = 0$  for baryonic and dark matter. As stated in  $\Lambda_{CDM}$  model,

that dark matter does not evolve and its value for  $w$  is constant at 0. But in this section we will also use that as a free parameter and test beyond that model.

So in order to express the energy,  $E(z)$ , of the universe in which  $w$  could vary, we use the continuity equation:

$$\dot{\rho} = -3(\rho + p)\frac{\dot{a}}{a} \quad (33)$$

Expressing the pressure,  $p$ , with equation(32) and integrating both side, we get:

$$\rho \propto a^{-3(1+w)} \quad (34)$$

and with the definition of redshift, this is:

$$\rho \propto (z + 1)^{3(1+w)} \quad (35)$$

We can insert this into equation(31) for different scenarios that require us to vary  $w$  for different cosmological fluids.

### 2.2.2 Constraining $\Omega_{m0}$ and $H_0$

This is the first scenario when our cosmology model haven't undergone modification yet. Meaning geometry is flat and with fixed  $w$ . Using (35) with  $w_{DM} = 0$  and  $w_{DE} = -1$ , the energy term for this cosmology is:

$$E(z) = \sqrt{(1 - \Omega_{m0}) + \Omega_{m0}(1 + z)^3} \quad (36)$$

With  $\Omega_{DE,0} = 1 - \Omega_{m0}$ .

One problem about constraining  $H_0$  here is that it is a local parameter, but for this simulation we are exploring into high redshift regime of up to 10, and we know that blackholes exists into higher redshift region.

### 2.2.3 Constraining $\Omega_{m0}$ and $w_{DE}$

In this part, the new parameter is  $w_{DE}$  and so  $H_0$  is kept constant here. It is worth mentioning that for each scenerio, we constrain 1 new parameter at a time. Combining with the existing parameters for population distribution then we have 9 in each scenario. So, any more than this then it would have been difficult for the parameters to constrain. Therefore, in this section and the rest,  $H_0$  is kept constant constant to the fiducial value.

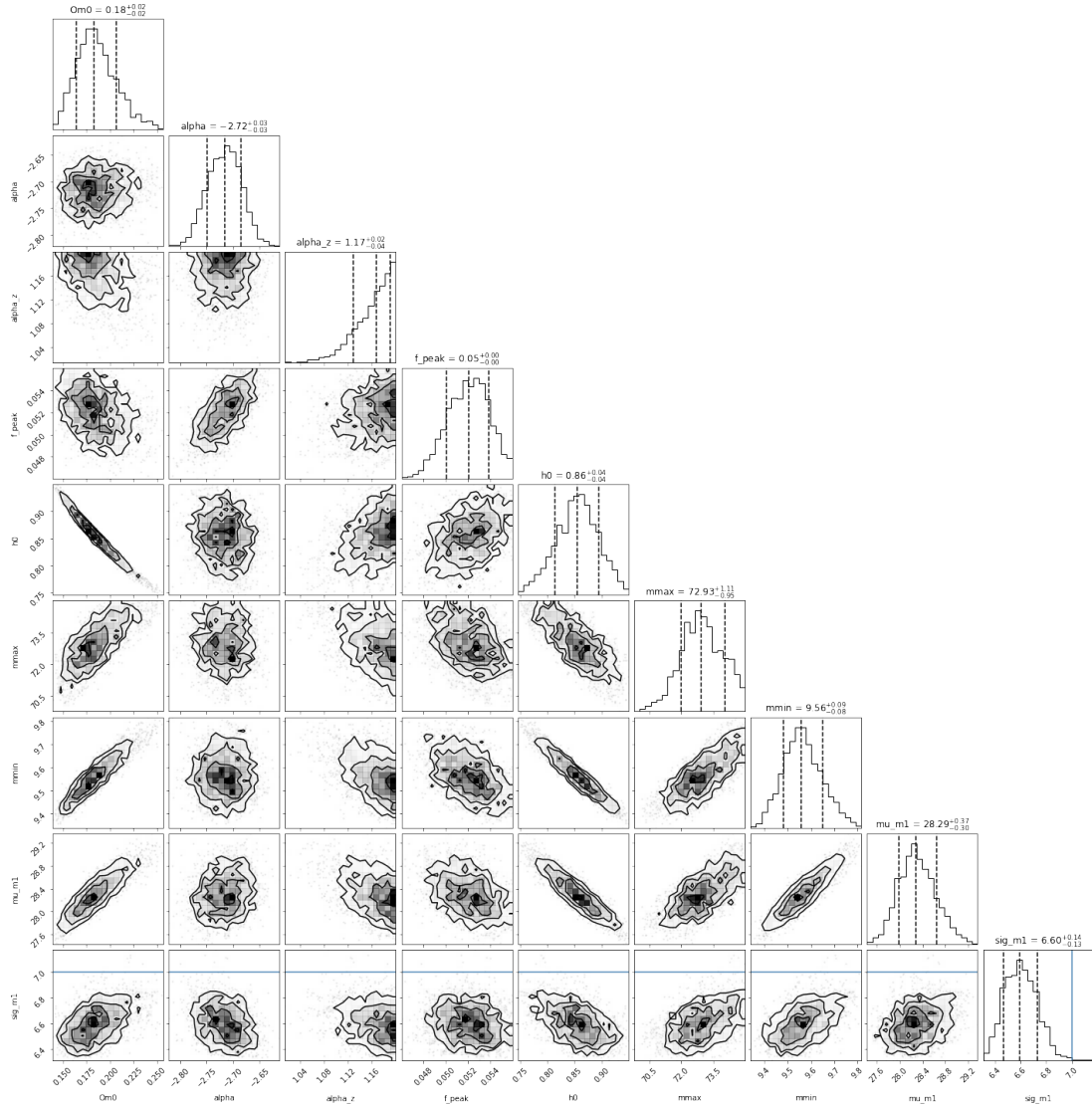


Figure 6: Corner plot for constraining the parameters of source distributions and cosmological parameters. Number of detections=20000. Name of parameters from top to bottom 1D histogram:  $Om_0$ ,  $\alpha$ ,  $\alpha_z$ ,  $f_{peak}$ ,  $h_0$ ,  $M_{max}$ ,  $M_{min}$ ,  $\mu$ ,  $\sigma$ . 2D histograms' x and y axis corresponds to the parameter names directly above and on the right of it. Blue line points to fiducial value but it does not always show up as most MCMC generated point don't always converge towards our fiducial value.

The expression of energy used in this one is:

$$E(z) = \sqrt{(1 - \Omega_{m0})(1 + z)^{3(1+w_{DE})} + \Omega_{m0}(1 + z)^3} \quad (37)$$

In which we have use the same method as above and  $w_{DE}$  now is a free parameter.

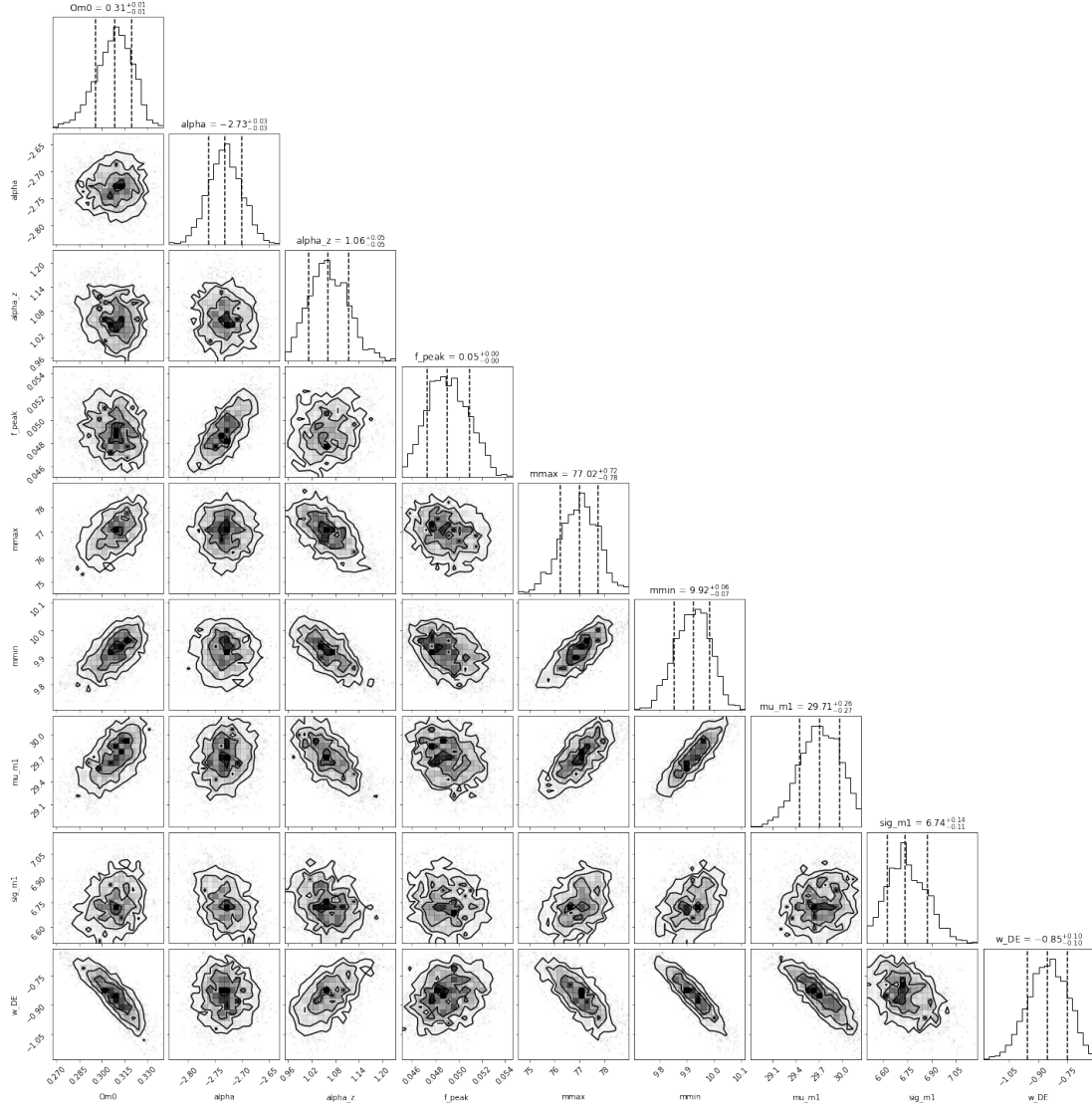


Figure 7: Corner plot for the original parameters plus  $w$  for dark energy. Number of detections= 20000. Name of parameters from top to bottom 1D histogram:  $Om0, \alpha, \alpha_z, f_{peak}, M_{max}, M_{min}, \mu, \sigma, w_{DE}$ . 2D histograms' x and y axis corresponds to the parameter names directly above and on the right of it.

## 2.2.4 Constraining $\Omega_{m0}$ and $w_{DM}$

The derivation for  $E(z)$  here is also the same as above, and with  $w_{DM}$  as a free parameter instead.

$$E(z) = \sqrt{1 - \Omega_{m0} + \Omega_{m0}(1+z)^{3(1+w_{DM})}} \quad (38)$$

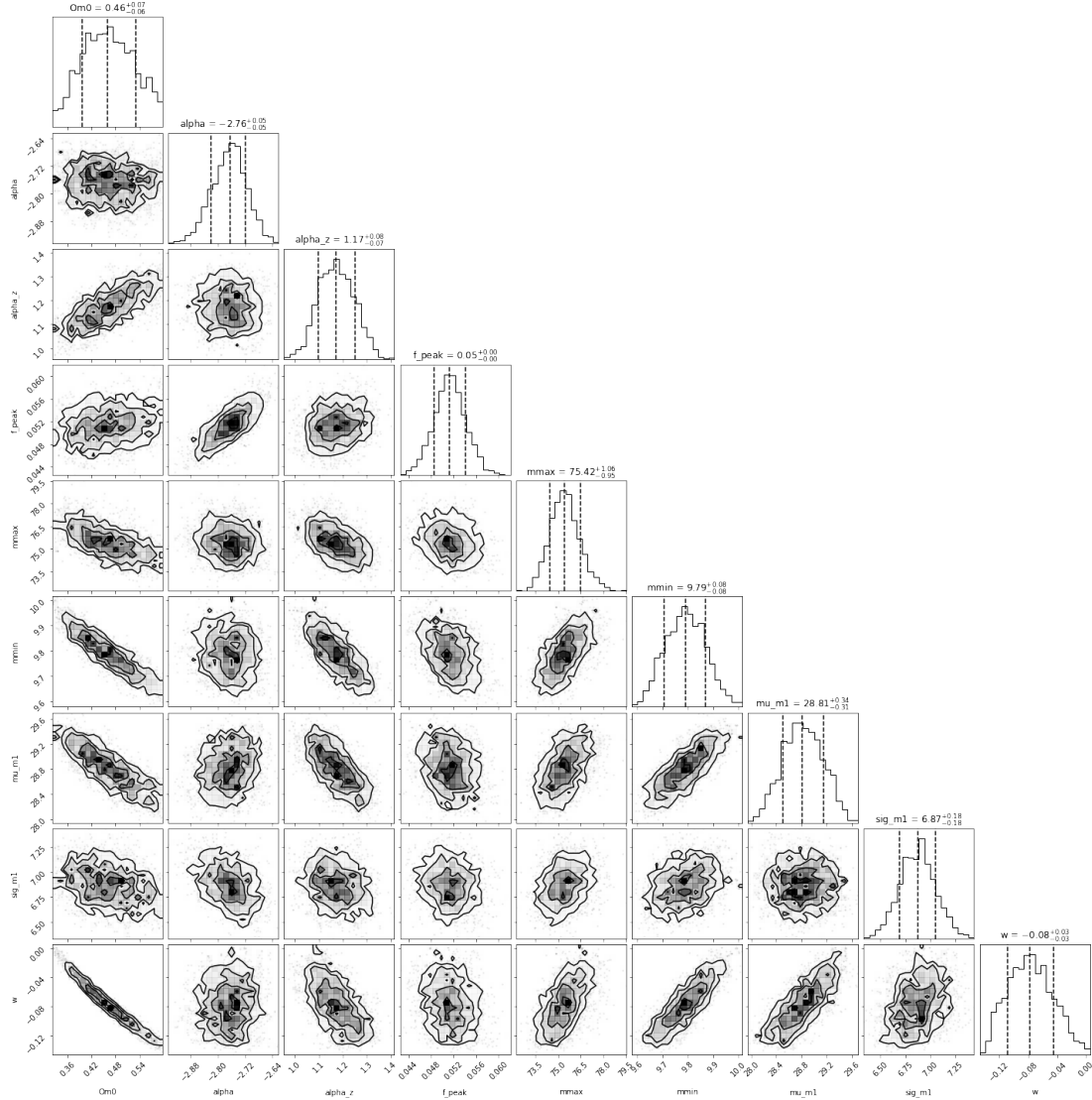


Figure 8: Corner plot for the original parameters plus  $w$  for dark matter. Number of detections = 5000. Name of parameters from top to bottom 1D histogram:  $Om0, \alpha, \alpha_z, f_{peak}, M_{max}, M_{min}, \mu, \sigma, w_{DM}$ . 2D histograms' x and y axis corresponds to the parameter names directly above and on the right of it.

### 2.2.5 Constraining $\Omega_{m0}$ and $\Omega_{k0}$

The energy expression used in this scenario is:

$$E(z) = \sqrt{\Omega_{DE} + \Omega_{m0}(1+z)^3 + \Omega_{k0}(1+z)^2} \quad (39)$$

The constraining of  $\Omega_{k0}$  in this section did not provide a physically valid result. All the MCMC walkers tried to rush beyond either  $\Omega_{k0} = -1$  or 1. Moreover, this scenario required the most modification out of all, in terms of the formula. For example changing  $d_L$  and  $d(dL)/dz$  to a version that could take  $-1 < \Omega_{k0} < 1$ . When the error happened, we adjusted the range and equations involving  $\Omega_{k0}$  to take only positive values. But it still return the same result. The detail of  $d_L$  and  $\partial(d_L)/\partial z$  could be referred to in the Appendix.

## 2.3 Results and Analysis

All the scenarios above were run with 2500 iteration steps to ensure walkers go beyond the effective number,  $N_{eff}$ , needed to get sufficient convergence from MCMC. Each run are repeated with increasing numbers of detection, from 5000 to 25000, in 5000 detection increments, and the evolution in error are investigated. The result are then presented in figure[9], where the constraint parameters are plotted as a function of number of measurements. Unfortunately we could not reach 25000 detections in simulation for  $w_{DE}$  and  $w_{DM}$  constraint, as the simulation takes extremely long- but this is sufficient enough to see a trend.

On the error of the simulation, theoretically should reduce as  $1/\sqrt{N}$  where  $N$  is the number of data points. From the plot, it is clear that the error decrease as number of measurement increase - but we do not have enough precision display of error from our program to tell how close the error follows the expected trend (i.e. error displayed is about 2 decimal points). It is also worth noting that, since the number of detections that we used in this simulation is on the scale of  $10^3 - 10^4$ , the result gained from this is more representative of next generation detectors such as Einstein Telescope or Cosmic Explorer, as stated in table 1.

For each simulation, corner and chain plots , along with their statistics were produced. These are useful because we could judge how well each parameters were constrained, or how even the distributions were. Most importantly, whether there were any divergents. So that in the next simulation run, the prior range could be adjusted so that it can constrain more towards a specific value. Doing this would improve the error significantly. Examples of corner plots of all parameters from each simulation scenarios are figure [6],[7],and [8]. One may notice that some of the 2D histograms(the one that is shaded) may not always have

round shapes- or they do but have some part cropped out, but one thing we tried to ensure of when generating these is that the important parameters i.e.  $\Omega_{m0}, w_{DE}, w_{DM}$  are unskewed and as symmetric as possible. As these are the signs of being well constrained.

By looking at each scenerios- the one where we converged  $w_{DM}$  may had the most stable and well-behaved corner plots, but in terms of individual parameters,  $\Omega_{m0}$  in the  $w_{DE}$  scenario is the most consistent across all number of detections. As shown in figure[9]. The value of this  $\Omega_{m0}$  is 0.31, which is approximately the same as our fiducial value ( even with error varies from 0.03 to 0.01). This could indicate that our simulation, at least in this scenario, has a good degree of accuracy.

## 2.4 Possible Improvement

There are multiple ideas for both future work and possible improvements for the project if there was more time, or if someone were to pick it up. The most obvious one would be to identify the error in the formulation for constraining  $\Omega_{k0}$ . Because this is one of the important elements of probing the standard model of cosmology. Secondly, since the constraining of  $w_{DE}$  and  $w_{DM}$  went decently, it is very much possible to upgrade them from being a constant, to  $w_{DE}$  that varies as a function of redshift. I.e.  $w_{DE}(z) = w_a z / (1 + z) - (w_0 + w_a)$ . [15][16]

## 3 Conclusion

Summarising the results we have worked so far: In part I, we have determined the rate of detections of LIGO O3,O4, VIRGO O5 and next generation detectors such as Einstein Telescope and Cosmic Explorer. Eventhough the results may have been an overestimation but it provided good context to how much more sensitivities can improve over the generations. Moreover, it helped determined in what detection scenario our simulation in part II would be relevant to - as we generated number of detections in the order of magnitude of  $10^3 - 10^4$ , it would definitely be a prediction for new generation telescope. Finally, the values of parameters we obtained from the bayesian inference program are consistent with fiducial values, especially with the accuracy of  $\Omega_{m0}$  in  $w_{DE}$  scenario. As well as the fact that all model showed the trend of getting less uncertainty as measurement increases. But most importantly we have certainly explored the possibility beyond the standard cosmological model.

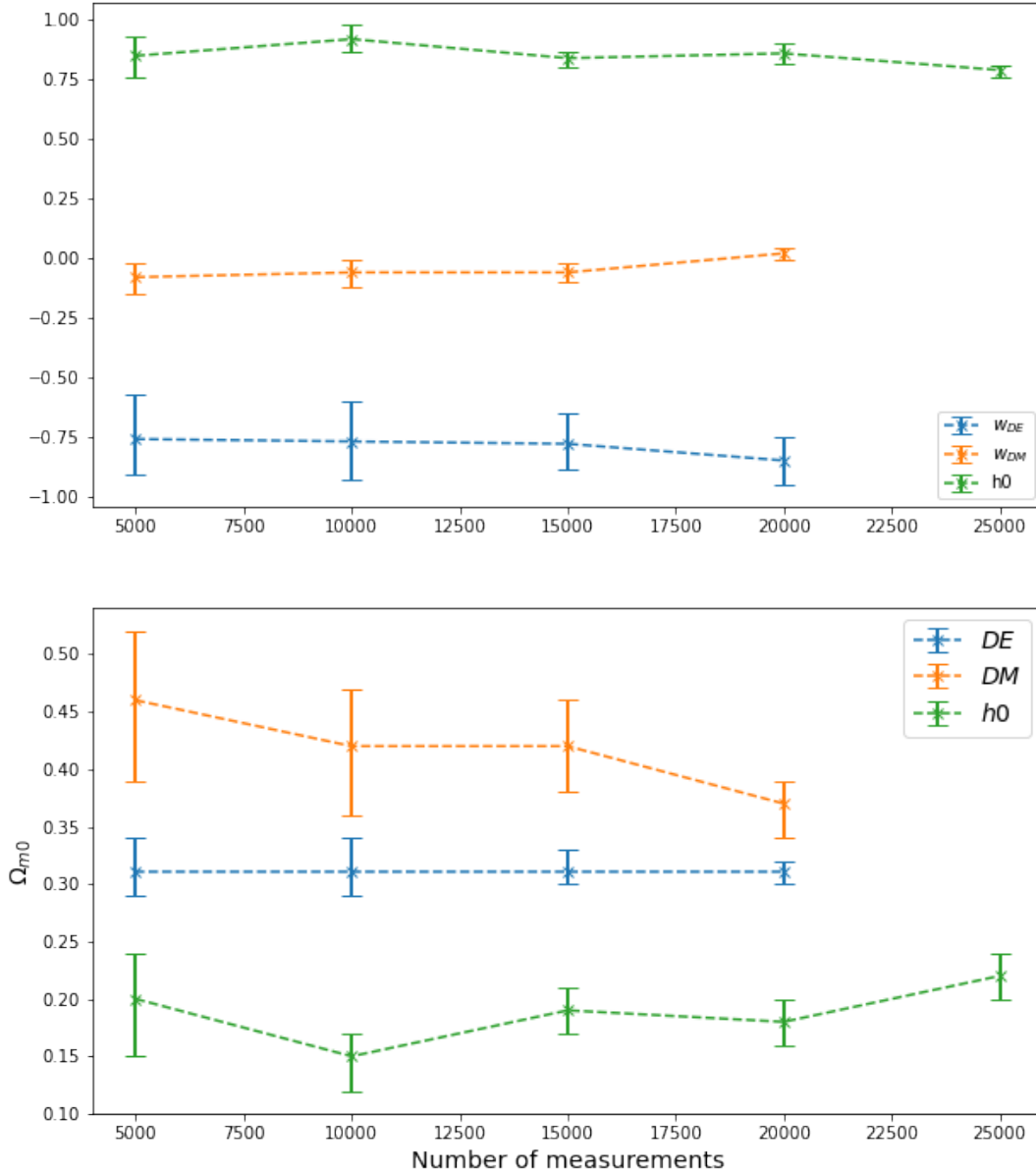


Figure 9: (Top): Values of converged cosmological parameters:  $w_{DE}$  in blue,  $w_{DM}$  in orange, and  $h_0$  in green. (Bottom): values for  $\Omega_{m0}$  in different simulation scenerios where they were converging with  $w_{DE}$ ,  $w_{DM}$ , and  $h_0$ . The x-axis for both subplots are the number of measurements

## 4 Appendix

### From section 1.3.2

The full description of mass distribution function, equation(23) is:

$$p(m) = \begin{cases} \Psi \times \exp \left[ - (m - M_{min})^2 / 2(\delta M_{min})^2 \right] & m < M_{min} \\ \Psi & M_{min} < m < M_{max} \\ \Psi \times \exp \left[ - (m - M_{max})^2 / 2(\delta M_{max})^2 \right] & m > M_{max} \end{cases} \quad (40)$$

With  $\delta M_{min} = 1, \delta M_{max} = 2$  And  $\Psi(\sigma, \mu, f_{peak})$  is just:

$$f_{peak} \times \left( \frac{1}{\sigma\sqrt{2\pi}} \exp \left[ -\frac{1}{2} \left( \frac{m - \mu}{\sigma} \right)^2 \right] \right) + (1 - f_{peak})(powerlaw)$$

### From section 2.2.5: Constraining $\Omega_{m0}$ and $\Omega_{k0}$

The equation for luminosity distance that replaces the normal expression for  $d_L$ . This one is in terms of measurable cosmological parameters, and curvature term[17]:

$$d_L(z) = (1 + z) \frac{cH_0^{-1}}{\sqrt{|\Omega_{k0}|}} S_k \left[ \sqrt{|\Omega_{k0}|} \int \frac{dz'}{E(z')} \right] \quad (41)$$

Where

$$S_k = \begin{cases} \sinh \left( \sqrt{|\Omega_{k0}|} \int \frac{dz'}{E(z')} \right) & \Omega_{k0} < 0 \\ \sqrt{|\Omega_{k0}|} \int \frac{dz'}{E(z')} & \Omega_{k0} = 0 \\ \sin \sqrt{|\Omega_{k0}|} \int \frac{dz'}{E(z')} & \Omega_{k0} > 0 \end{cases} \quad (42)$$

## References

- [1] M. Evans et al, (2021), Cosmic Explorer Technical Report CE–P2100003–v7
- [2] T. Harmark,(2021), General Relativity and Cosmology Lecture notes, NBI
- [3] I. Tamborra,(2022), Fundamentals of High-Energy Astrophysics and Particle Astrophysics lecture note , Niels Bohr International Academy and DARK
- [4] B.S. Sathyaprakash, B.F. Schutz,(2009), Physics, Astrophysics and Cosmology with Gravitational Waves, p. 27, arXiv:0903.0338 [gr-qc]
- [5] LIGO facts from the official LIGO website. <https://www.ligo.caltech.edu/page/facts>
- [6] G. Pratten et al, (2021) Setting the cornerstone for the IMRPhenomX family of models for gravitational waves from compact binaries: The dominant harmonic for non-precessing quasi-circular black holes
- [7] M. Maggiore, Gravitational Waves Volume 1: Theory and Experiments
- [8] P. Madau, M. Dickinson, (2014), Cosmic Star-Formation History, P.48
- [9] R. Abbott, T. D. Abbott et al., (2022), The population of merging compact binaries inferred using gravitational waves through GWTC-3, P.46
- [10] H. Chen et al,(2021) DISTANCE MEASURES IN GRAVITATIONAL-WAVE ASTROPHYSICS AND COSMOLOGY, Sec 4.2
- [11] J.M. Ezquiaga, D. E. Holz,(2021), Jumping the gap: searching for LIGO’s biggest black holes
- [12] I. Mandel, W. M. Farr, J. R. Gair, (2019), Extracting distribution parameters from multiple uncertain observations with selection biases
- [13] Jeremy Orloff, Jonathan Bloom, (2014), Introduction To Probability And Statistics, Reading 17a: The Frequentist School of Statistics, MITOpenCourseWare
- [14] Planck Collaboration, (2021), Planck 2018 results. VI. Cosmological parameters, ESO
- [15] Hsin-Yu Chen, Tests of LCDM from WP perspective: methods and pipelines, Fundamental Physics with LISA, August 2023, <https://strong-gr.com/documents/19/Hsin-Yu.pdf>

[16] D.E. Holz, S. A. Hughes, (2008), USING GRAVITATIONAL-WAVE STANDARD SIRENS

[17] S. M. Carroll, An Introduction to General Relativity Spacetime and Geometry, Ch.8, eq 8.123